chemosensors

MDPI

Article

A Rationally Designed, Spiropyran-Based Chemosensor for Magnesium

Georgina M. Sylvia [1], Adrian M. Mak [2], Sabrina Heng [1,*], Akash Bachhuka [1], Heike Ebendorff-Heidepriem [1] and Andrew D. Abell [1,*]

[1] ARC Centre of Excellence for Nanoscale BioPhotonics, Department of Chemistry, Institute for Photonics and Advanced Sensing, The University of Adelaide, Adelaide SA 5005, Australia; georgina.sylvia@adelaide.edu.au (G.M.S.); akashbachhuka01@adelaide.edu.au (A.B.); heike.ebendorff@adelaide.edu.au (H.E.-H.)

[2] Institute of High Performance Computing, 1 Fusionopolous Way, No. 16-16 Connexis, Singapore 138632, Singapore; makwk@ihpc.a-star.edu.sg

* Correspondence: sabrina.heng@adelaide.edu.au (S.H.); andrew.abell@adelaide.edu.au (A.D.A.); Tel.: +61-8-8313-5652 (A.D.A.)

Received: 8 March 2018; Accepted: 16 April 2018; Published: 17 April 2018

Abstract: Magnesium ions (Mg^{2+}) play an important role in mammalian cell function; however, relatively little is known about the mechanisms of Mg^{2+} regulation in disease states. An advance in this field would come from the development of selective, reversible fluorescent chemosensors, capable of repeated measurements. To this end, the rational design and fluorescence-based photophysical characterisation of two spiropyran-based chemosensors for Mg^{2+} are presented. The most promising analogue, chemosensor **1**, exhibits 2-fold fluorescence enhancement factor and 3-fold higher binding affinity for Mg^{2+} (K_d 6.0 μM) over Ca^{2+} (K_d 18.7 μM). Incorporation of spiropyran-based sensors into optical fibre sensing platforms has been shown to yield significant signal-to-background changes with minimal sample volumes, a real advance in biological sensing that enables measurement on subcellular-scale samples. In order to demonstrate chemosensor compatibility within the light intense microenvironment of an optical fibre, photoswitching and photostability of **1** within a suspended core optical fibre (SCF) was subsequently explored, revealing reversible Mg^{2+} binding with improved photostability compared to the non-photoswitchable Rhodamine B fluorophore. The spiropyran-based chemosensors reported here highlight untapped opportunities for a new class of photoswitchable Mg^{2+} probe and present a first step in the development of a light-controlled, reversible dip-sensor for Mg^{2+}.

Keywords: magnesium chemosensor; photoswitchable; spiropyran; merocyanine; fluorescent chemosensor; microstructured optical fibre; suspended core fibre

1. Introduction

Magnesium ions (Mg^{2+}) play an important role in mammalian cell function [1–4], as an enzymatic cofactor [5], regulator of cellular ion channels [6–8] and energy metabolism [9]. Conditions such as Type 2 Diabetes [10–12], Alzheimer's [13,14] and cardiovascular disease [15,16] have been linked with magnesium deficiency, however the mechanisms of Mg^{2+} regulation in such disease states are poorly understood [17,18]. Fluorescent chemosensors, in combination with specialised imaging technologies, provide a useful tool to study the role of metal ions in cellular processes as they enable detection in and around cells with spatial and temporal resolution [19].

Mag-fura-2 (FURAPTRA) [20,21] is one such commercially available chemosensor for Mg^{2+}, based on a benzofuran fluorophore scaffold and functionalised with the *O*-aminophenol-*N*,*N*,*O*-triacetic

acid (APTRA) Mg^{2+} chelator [22]. Mag-fura-2 has been shown to detect cytosolic Mg^{2+} in various cells [23–25], however as it is structurally analogous to the calcium (Ca^{2+}) chelator fura-2, intracellular Mg^{2+} detection is complicated by an affinity for Ca^{2+} [26,27]. More recently, other probes based on fluorophore scaffolds such as fluorescein and rhodamine have been reported to display improved selectivity [28–30]. For example, the KMG series of chemosensors possess a bidentate, charged beta-diketone binding domain, which gives rise to excellent Mg^{2+} selectivity over Ca^{2+} (Figure 1B) [29]. Similar selectivity has been observed with the MGQ series, which possess a range of tridentate carboxy binding domains (Figure 1C) [30]. These studies represent significant developments in the field of Mg^{2+} detection, but further work is required in order to advance this area [31,32].

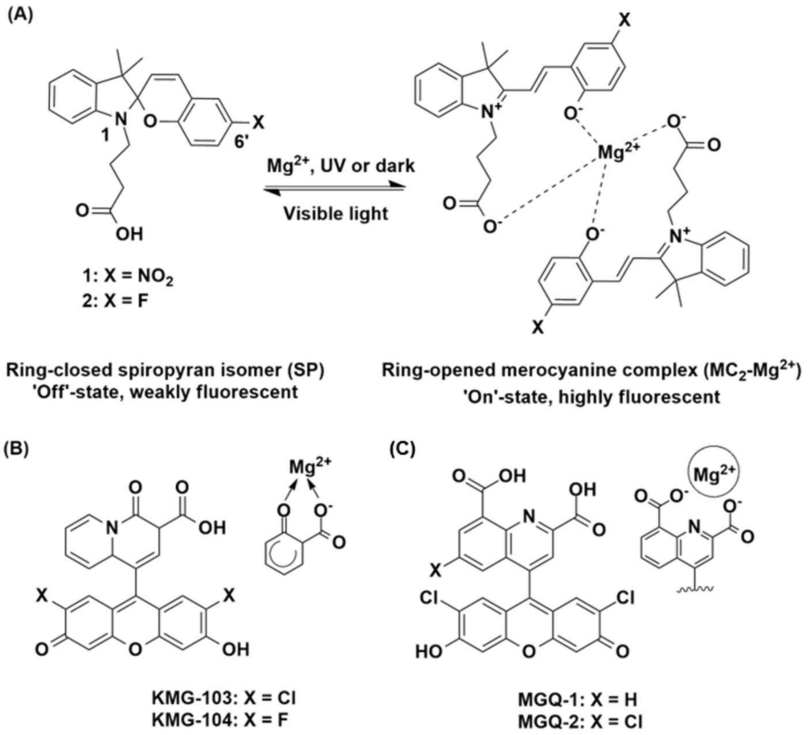

Figure 1. (**A**) Structures of **1** and **2** as the ring-closed, weakly fluorescent spiropyran (SP, 'off') isomer, and the proposed ring-opened, highly fluorescent merocyanine (MC_2-Mg^{2+}, 'on') complex. Structures of the (**B**) KMG [29] and (**C**) MGQ [30] chemosensors with the proposed Mg^{2+}-binding domains highlighted.

For example, the ability to turn metal ion sensing on and off, with an external and non-invasive stimulus such as light, would extend the range of sensing capability for live-cell imaging. A photoswitchable spiropyran presents as one such sensing moiety, where these structures form the basis of a chemosensor when functionalised with a suitable ionophore that is capable of complexing with a metal ion [33,34]. Photo-controlled switching between the weakly fluorescent spiropyran (SP) and highly fluorescent merocyanine (MC) isomers occurs on irradiation with UV light or in the presence of the target metal ion, while visible light reverses the isomerisation (see **1** and **2** Figure 1A) [35–37]. Recently, we have reported the combination of spiropyran-based chemosensors with microstructured optical fibres for the nanoscale detection of metal ions [38–40]. These systems have been shown to yield significant signal-to-background changes with minimal sample volumes, a real advance in biological sensing that enables measurement on subcellular-scale samples. Importantly, spiropyrans are among the most stable photoswitches in the light intense microenvironment of an optical fibre [41]. The fibre also provides a platform for sensing metal ions in confined spaces such as the medium surrounding cell clusters, oocytes and embryos, and in the in vivo environment [42–44].

Here we present two rationally designed, spiropyran-based chemosensors for Mg^{2+} (**1** and **2**, Figure 1A). Chemosensor **1** consists of a photoswitchable spiropyran fluorophore scaffold, functionalised with a butanoic acid at the N1-indole. The molecule is designed to chelate Mg^{2+} through the free carboxyl group, in combination with the phenoxide of the ring-opened merocyanine isomer. We envisaged that **1** would bind Mg^{2+} in a 2:1 chemosensor to metal ion ratio (depicted in Figure 1A), in a design inspired by the Mg^{2+}-selective, literature chemosensors described above [28–30]. An electron withdrawing NO_2 group was incorporated at the C6′ position of the benzopyran ring, since such groups are known to further promote metal ion binding by stabilising the ring-opened MC isomer [45]. The fluorinated analogue **2** was also investigated as a moderately electron withdrawing fluoro-substituent is known to give rise to relatively high fluorescence yields compared to a nitro analogue [39]. It is interesting to note that while absorbance-based photophysical studies have previously been reported on **1** [33,46], the fluorescence properties of this chemosensor in the presence of Mg^{2+} are unknown. As such, this work reports on the rational design and photophysical characterisation of the first spiropyran-based fluorescence chemosensors for Mg^{2+} and demonstrates the photo-compatibility of chemosensor **1** within a suspended core optical fibre (SCF) as a first step in the development of a light-controlled, reversible dip-sensor for Mg^{2+}.

2. Materials and Methods

All ^{13}C-NMR and ^{1}H-NMR spectra were recorded on an Agilent Technologies 500 MHz NMR with DD2 console in CD_3CN or DMSO-d_6 (Cambridge Isotope Laboratories, Cambridge, MA, USA). Chemical shifts (δ) are reported in ppm. Chemical shifts of CD_3CN (δ_C = 118.26 ppm), DMSO-d_6 (δ_C = 39.52 ppm) or TMS (δ_H = 0.0 ppm) were used as internal standards in all ^{13}C-NMR and ^{1}H-NMR experiments, respectively. High resolution mass spectrometry was performed on the Agilent 6230 TOF LC-MS. HPLC grade acetonitrile was used in all related experiments. All metal ions used in this work were in the form of perchlorate salt, except for Cs_2SO_4. All reagents were purchased from Sigma-Aldrich (St. Louis, MO, USA) and used without further purification.

2.1. Chemical Syntheses

2.1.1. Ethyl 4-(3′,3′-Dimethyl-6-fluorospiro[chromene-2,2′-indolin]-1′-yl)butanoate (**4**)

To a solution of 5-fluoro-2-hydroxybenzaldehyde **8** (44 mg, 0.31 mmol) in dry ethanol (5 mL) was added 1-(4-ethoxy-4-oxobutyl)-2,3,3-trimethyl-3H-indolium bromide **6** (100 mg, 0.28 mmol) and the reaction heated at reflux for 18 h. The solvent was removed in vacuo to give an orange crude oil (150 mg). The crude compound was purified on normal-phase silica by gradient column chromatography in 0–10% methanol in dichloromethane to give **4** as a yellow oil (44 mg, 39%). ^{1}H-NMR (500 MHz, DMSO-d_6) δ 7.10–7.06 (m, 3H, Ar*H*), 6.97 (d, 1H, Ar*H*, *J* = 10.5 Hz), 6.90 (td, 1H, Ar*H*, *J* = 8.5, 3.5 Hz), 6.75 (t, 1H, Ar*H*, *J* = 7.5 Hz), 6.65 (dd, 1H, Ar*H*, *J* = 8.5, 4.5 Hz), 6.61 (d, 1H, Ar*H*, *J* = 8.0 Hz), 5.84 (d, 1H, Ar*H*, *J* = 7.5 Hz), 4.00 (q, 2H, CH_2, *J* = 7.5 Hz), 3.19–3.12 (m, 1H, C*H*H), 3.10–3.04 (m, 1H, CH*H*), 2.35–2.30 (m, 2H, CH_2), 1.86–1.80 (m, 1H, C*H*H), 1.78–1.72 (m, 1H, CH*H*), 1.19 (s, 3H, CH_3), 1.13 (t, 3H, CH_3, *J* = 7.5 Hz), 1.07 (s, 3H, CH_3) ppm; ^{13}C-NMR (126 MHz, DMSO-d_6) δ 172.6, 156.8, 155.0, 149.8, 147.0, 135.9, 128.5, 128.4, 127.4, 121.6, 121.1, 118.6, 112.9, 112.7, 106.3, 104.3, 59.7, 51.8, 42.3, 31.0, 25.7, 23.7, 19.7, 14.0 ppm; HRMS-ESI (*m*/*z*) calculated for $C_{24}H_{26}FNO_3$ $[M + Na]^+$ 418.1789, found 418.1769.

2.1.2. Ethyl 4-(3′,3′-Dimethyl-6-nitrospiro[chromene-2,2′-indolin]-1′-yl)butanoate (**3**)

To a solution of 2-hydroxy-5-nitrobenzaldehyde **7** (52 mg, 0.31 mmol) in dry ethanol (5 mL) was added **6** (100 mg, 0.28 mmol) and the solution heated at reflux for 18 h. The solvent was removed in vacuo to give a brown crude solid (156 mg). The crude compound was purified on normal-phase silica by gradient column chromatography in 0–10% methanol in dichloromethane to give **3** as a purple solid (64 mg, 54%). ^{1}H-NMR (500 MHz, DMSO-d_6) δ 8.21 (d, 1H, Ar*H*, *J* = 3.0 Hz,), 7.99 (dd, 1H, Ar*H*, *J* = 2.5, 8.5 Hz), 7.20 (d, 1H, Ar*H*, *J* = 10.0 Hz), 7.13–7.10 (m, 2H, Ar*H*), 6.85 (d, 1H, Ar*H*, *J* = 9.0 Hz), 6.79 (t,

1H, Ar*H*, *J* = 7.5 Hz), 6.66 (d, 1H, Ar*H*, *J* = 8.0 Hz), 5.98 (d, 1H, Ar*H*, *J* = 10.0 Hz), 4.00 (q, 2H, CH_2, *J* = 7.0 Hz), 3.20–3.10 (m, 2H, CH_2), 2.36–2.30 (m, 2H, CH_2), 1.86–1.81 (m, 1H, C*H*H), 1.76–1.71 (m, 1H, CH*H*), 1.19 (m, 3H, CH_3), 1.13–1.09 (m, 6H, 2 × CH_3) ppm; ^{13}C-NMR (126 MHz, DMSO-d_6) δ 172.6, 159.1, 146.7, 140.5, 135.6, 129.6, 128.1, 127.6, 125.7, 122.8, 121.7, 121.6, 119.1, 115.4, 106.5, 106.4, 59.8, 52.3, 42.3, 30.9, 25.8, 23.6, 19.6, 14.0 ppm; HRMS-ESI (m/z) calculated for $C_{24}H_{26}N_2O_5$ found $[M + Na]^+$ 445.1734, found 445.1720.

2.1.3. 4-(6-Fluoro-3′,3′-dimethylspiro[chromene-2,2′-indolin]-1′-yl)butanoic acid (**2**)

To a solution of **4** (200 mg, 0.51 mmol) in methanol (10 mL) was added 2 M aqueous NaOH (5 mL) and the reaction heated at 50 °C for 5 h. The solvent was removed in vacuo to give an orange solid (1.362 g). A sample of the crude material (100 mg) was purified by reverse-phase HPLC eluting water and acetonitrile (60–100%) to give a purple solid consisting of **2** in mixture with its MC isomer (41 mg); ^{1}H-NMR (500 MHz, CD_3CN/DMSO-d_6) selected data for SP isomer from mixture δ 7.08–6.48 (m, arom*H*), 6.84 (d, 1H, C*H*, *J* = 10.0 Hz), 5.83 (d, 1H, C*H*, *J* = 10.0 Hz), 3.18–3.12 (m, 2H, CH_2), 2.31 (d, 2H, CH_2, *J* = 8.0 Hz), 1.74–1.69 (m, CH_2), 1.18 (s, 3H, CH_3), 1.06 (s, 3H, CH_3); selected data for the MC isomer from mixture δ 7.08–6.48 (m, arom*H*), 4.46 (d, 1H, C*H*H, *J* = 10.0 Hz), 4.12 (m, 1H, CH*H*), 2.06–2.03 (m, 2H, CH_2), 1.74–1.69 (m, CH_2), 1.23 (s, 3H, CH_3), 1.19 (s, 3H, CH_3); HRMS-ESI (m/z) calculated for $C_{22}H_{22}FNO_3$ $[M + H]^+$ 368.1656, found 368.1646.

2.1.4. 4-(3′,3′-Dimethyl-6-nitrospiro[chromene-2,2′-indolin]-1′-yl)butanoic acid (**1**)

To a solution of **3** (224 mg, 0.53 mmol) in methanol (10 mL) was added 2M aqueous NaOH (5 mL) and the reaction heated at 50 °C for 5 h. The solvent was removed in vacuo to give an orange solid (1.441 g). The crude material was purified by reverse-phase HPLC eluting with water and acetonitrile (60–100%) to give **1** as an orange solid (104 mg, 50%). ^{1}H-NMR (500 MHz, CD_3CN) δ 8.06 (d, 1H, Ar*H*, *J* = 2.5 Hz,), 7.98 (dd, 1H, Ar*H*, *J* = 3.0, 9.0 Hz), 7.14 (t, 1H, Ar*H*, *J* = 7.5 Hz), 7.10 (d, 1H, Ar*H*, *J* = 10.0 Hz), 7.02 (d, 1H, Ar*H*, *J* = 10.0 Hz), 6.83 (t, 1H, Ar*H*, *J* = 7.5 Hz), 6.70 (d, 1H, Ar*H*, *J* = 9.0 Hz), 6.68 (d, 1H, Ar*H*, *J* = 7.5 Hz), 5.96 (d, 1H, Ar*H*, *J* = 10.5 Hz), 3.24–3.11 (m, 2H, CH_2), 2.31–2.27 (m, 2H, CH_2), 1.92–1.76 (m, 2H, CH_2), 1.24 (s, 3H, CH_3), 1.14 (s, 3H, CH_3) ppm; ^{13}C-NMR (126 MHz, CD_3CN) δ 174.6, 160.4, 148.2, 142.1, 137.10, 129.1, 128.7, 126.6, 123.7, 122.8, 122.7, 120.4, 120.0, 116.2, 107.9, 107.8, 53.3, 43.6, 31.5, 26.3, 24.7, 20.00 ppm; HRMS-ESI (m/z) calculated for $C_{22}H_{22}N_2O_5$ $[M + H]^+$ 395.1579, found 395.1587.

2.2. Spectroscopic Analyses of Chemosensors **1**–**4**

Stock solutions of spiropyrans (5 mM) were prepared in HPLC-grade acetonitrile. Stock solutions of metal ion salts (10 mM) were prepared in water from dried perchlorate salts of Li^+, Na^+, K^+, Mg^{2+}, Ca^{2+}, Mn^{2+}, Cu^{2+}, Zn^{2+}, and Cs^+ (from Cs_2SO_4). For the selectivity studies, solutions were prepared (in triplicate) on the same microplate tray from 2 μL spiropyran and 2 μL of ion stock solutions, such that each replicate contained a 2:1 molar ratio of ion: spiropyran. 196 μL of HPLC grade acetonitrile was then added to dilute each replicate, such that the final concentrations of spiropyran and ions in each solution were 50 μM and 100 μM, respectively. The microplate tray was then incubated in the dark for 10 mins before reading. Absorbance and fluorescence spectra were recorded between 300 and 700 nm, and 555 and 800 nm, respectively, at 25 °C using a BioTek Synergy H4 Hybrid Multi-Mode Microplate Reader. The scanning resolution was 5 nm, with a band pass of 9 nm. Fluorescence excitation was at 532 nm, with 100 gain setting for all chemosensors. All absorbance and fluorescence measurements were repeated in triplicate. The error bars presented represent a standard deviation about the mean value. Further details of the solution-based fluorescence experiments are reported in the Supporting Information.

2.3. Photoswitching in Optical Fibre

A 5 mW laser was coupled into the core of a suspended core fibre (SCF) via dichroic mirror at a wavelength of 532 nm using 60× objective as described previously [39]. One end of the fibre was filled by capillary action by dipping in an acetonitrile solution containing chemosensor **1** (500 μM) and Mg^{2+} (1 mM). The chemosensor-filled SCF was then exposed to a 532 nm green laser for 2 min, and fluorescence was measured after excitation with the same 532 nm laser (10 × 50 ms). Next, the SCF was exposed to UV light (365 nm) for 5 min to facilitate photoswitching to the ring-opened MC(**1**)-Mg^{2+} complex, and fluorescence was measured again after excitation with the 532 nm green laser (10 × 50 ms). This process was repeated for 10 cycles to investigate photoswitching of **1** in the presence of Mg^{2+}. Fluorescence of Rhodamine B was similarly recorded; however, UV irradiation was not required for the 'on' cycles as this fluorophore does not photoswitch.

3. Results and Discussion

3.1. DFT Modelling

Structures of chemosensors **1** and **2**, bound with both Mg^{2+} and Ca^{2+}, were calculated by density functional theory based on a 2:1 binding of ring opened merocyanine isomer to metal ion (see Figure 1). This proposed coordination geometry has precedent for similarly functionalised spiropyran-based chemosensors with divalent metal ions [47–49]. Two water molecules were included in the initial calculations to provide additional coordinating sites, based on the metal-bound crystal structure reported for a similar spiropyran [47]. Geometry optimised structures were obtained using the B3LYP functionals [50] and 6-311G** basis set for all atoms, within the Gaussian09 package [51].

The optimised structures for chemosensor **1** bound to Mg^{2+} and Ca^{2+} are presented in Figure 2. The resulting complexes of **1** bound with Mg^{2+} and Ca^{2+} are both hexa-coordinated, such that the ion is bound by two, bidentate MC ligands, with two water molecules fulfilling the coordination of the metal in each case. The $Mg^{2+}\cdots O$ distances are between 2.07 and 2.13 Å, and $Ca^{2+}\cdots O$ distances are between 2.37 and 2.46 Å. The reaction energies for the formation of the M[**1**$(MC)_2(H2O)_2$] species were calculated to be −299.0 kJ/mol and −137.8 kJ/mol for Mg^{2+} and Ca^{2+}, respectively. Similar results were observed for the fluorinated chemosensor **2** (see Figure S9). Taken together, the more negative ΔG_{298} for the formation of the Mg[**1**$(MC)_2(H2O)_2$] and Mg[**2**$(MC)_2(H2O)_2$], and the shorter $Mg^{2+}\cdots O$ distances compared with Ca^{2+} analogues in this study suggest stronger binding of the Mg^{2+} compared to the Ca^{2+} by chemosensors **1** and **2**.

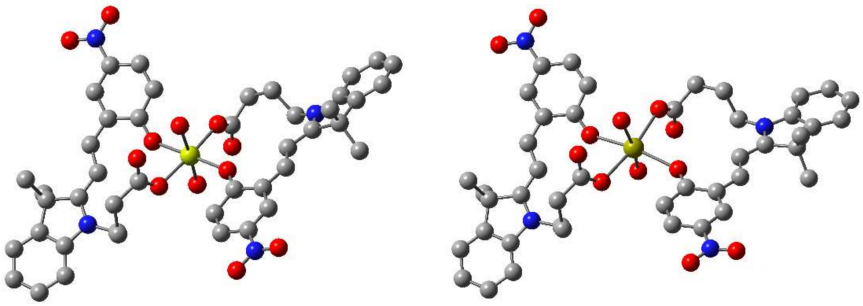

(**A**) (**B**)

Figure 2. B3LYP/6-311G** optimised structure of **1** bound to (**A**) Mg^{2+} (yellow) and (**B**) Ca^{2+} (gold), respectively, in a 2:1 ratio, showing oxygen atoms (red) chelating to the metal ion. Hydrogen atoms are omitted for clarity.

3.2. Synthesis

Compounds **1** and **2** were prepared as outlined in Scheme 1. Commercially available 3,3-dimethyl-2-methyleneindoline **5** was alkylated with ethyl-4-bromobutanoate to give the previously reported indoline **6** [38]. Separate condensation reactions of 2-hydroxy-5-nitrobenzaldehyde **7** or 5-fluoro-2-hydroxybenzaldehyde **8**, with indoline **6** in refluxing ethanol, gave the ester-protected spiropyrans **3** and **4,** respectively which were fully characterised by ^{1}H, ^{13}C-NMR and HRMS (see Figures S1–S4 and S8). Spiropyrans **3** and **4** were then separately treated with 2 M aqueous NaOH in order to hydrolyse the ester protecting groups, and the crude, free-acid products were then purified by reverse-phase HPLC, respectively. The resulting compounds were characterised by ^{1}H, ^{13}C-NMR and HRMS, with details reported in Supporting Information (Figures S5–S8). The proton NMR spectrum of **1** shows the chemosensor fully in the ring-closed SP form, as is consistent with previous studies [33]. Interestingly, the proton NMR spectrum of **2** suggests a mixture of SP and MC isomers. Based on this, subsequent work was focused on chemosensor **1**.

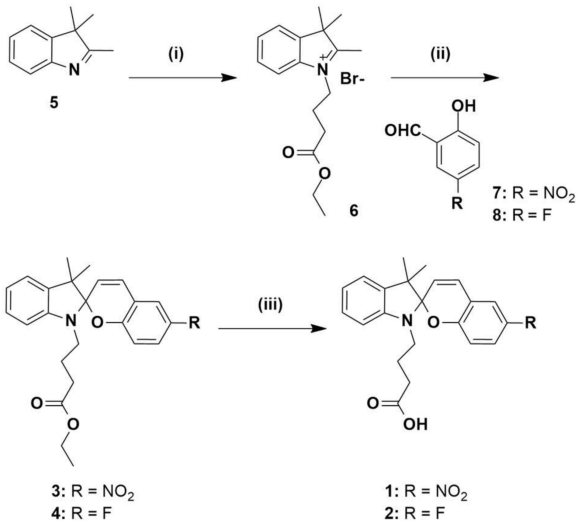

Scheme 1. Synthesis of chemosensors **1** and **2**. Reagents and conditions: (i) ethyl-4-bromobutyrate, $CHCl_3$, reflux 24 h; (ii) EtOH, reflux 18 h; (iii) 2 M NaOH, MeOH, 50 °C, 5 h.

3.3. Sensor Characterisation

Absorbance and fluorescence emission spectra of chemosensor **1** (50 μM in acetonitrile) were first measured in the presence of an excess of Mg^{2+} (100 μM), as well as other biologically relevant metal ions (Li^{+}, Na^{+}, K^{+}, Cs^{+}, Ca^{2+}, Mn^{2+}, Cu^{2+} and Zn^{2+}), to characterise its selectivity profile. Spectra were recorded in ambient light conditions, in order to characterise the metal-induced SP to MC isomerisation [36,37]. Results displayed in Figure 3 show that chemosensor **1** has the highest fluorescence emission in the presence of Mg^{2+}, 2-fold higher than that of Ca^{2+} and 3–4-fold higher than for Li^{+} and Zn^{2+}. In the presence of excess Mg^{2+}, **1** gives an emission maximum at 590 nm, hypsochromically shifted compared to the chemosensor in the presence of Ca^{2+} (605 nm) or in the absence of metal ions (605 nm). These maxima are characteristic of the MC-form of the spiropyran, and thus, metal ion binding induces isomerisation of chemosensor **1** to the more coloured MC(**1**)-M^{2+} complex [36]. As has been reported previously [33], chemosensor **1** exhibits a significant increase in the characteristic MC absorbance in the prescence of Cu^{2+} (Figure S10), while the absorbance spectra of the **1**-Mg^{2+} and **1**-Ca^{2+} species are similar to the SP form of **1** under ambient light conditions (see Figure 3A) [36].

Data pertaining to the photophysical characterisation of chemosensor **1** is presented in Table 1. The binding stoichiometry of **1** in the presence of excess Mg^{2+} was next defined by Job's plot analysis,

as displayed in Figure 3C. Chemosensor **1** binds Mg^{2+} in a 2:1 ratio (Job's plot apex at 0.33), in agreement with the design proposal and DFT modelling discussed above. Similarly, Job's analysis showed that **1** also binds Ca^{2+} in a 2:1 ratio (apex at 0.33, Figure S11). Dissociation constants (K_d) for the binding of **1** with Mg^{2+} and Ca^{2+}, respectively, were determined by fitting a saturation binding model to concentration curves of the chemosensor (50 μM) with increasing concentrations of metal ions (1–200 μM) (Figure S12). The dissociation constant for chemosensor **1** with Mg^{2+} was calculated to be 6.0 μM, and a 3-fold weaker affinity was observed with Ca^{2+} (K_d = 18.7 μM). Finally, the quantum yields of fluorescence for chemosensor **1** in the presence of Mg^{2+} (Φ = 0.20) and Ca^{2+} (Φ = 0.06) were determined via the method described in the Supporting Information, using Rhodamine B as the calibration standard (Figure S13) [52].

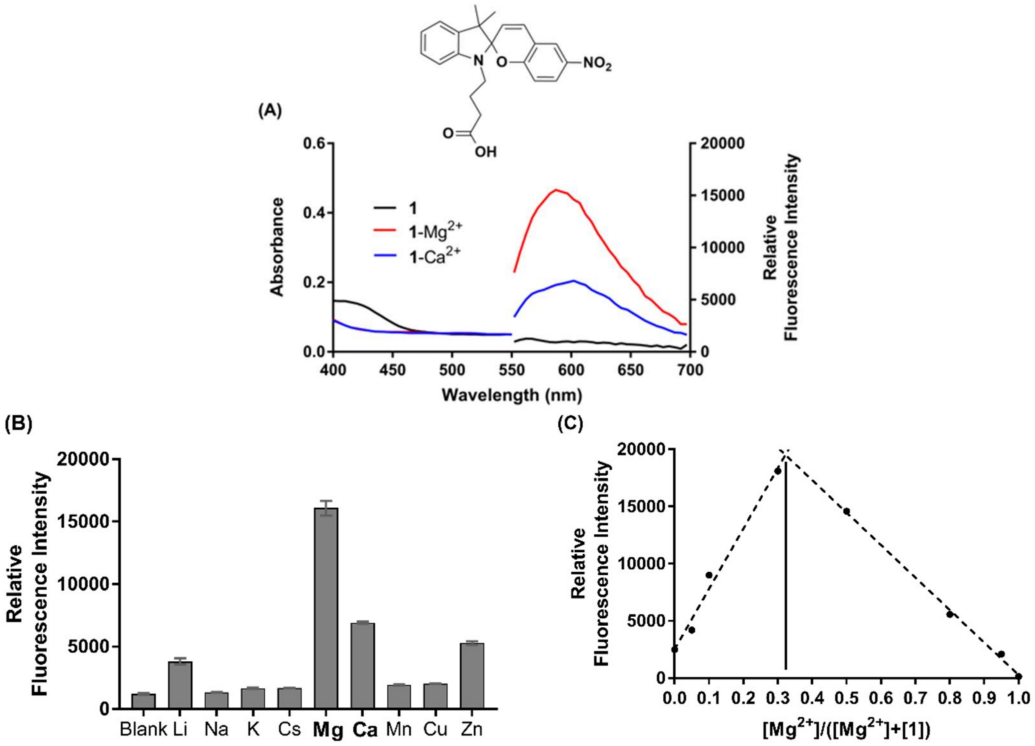

Figure 3. (**A**) Absorbance and fluorescence emission spectra of chemosensor **1** in the absence (black, 50 μM) and presence of excess Mg^{2+} (red, 100 μM) and Ca^{2+} (blue, 100 μM), respectively. (**B**) Selectivity profile of **1** (50 μM) in the presence of various biologically relevant metal ions (100 μM). (**C**) Job's plot analysis of MC(**1**)-Mg^{2+} complex, where [SP] + [Mg^{2+}] = 100 μM in acetonitrile. Excitation was at 532 nm, and all experiments were performed under ambient light conditions.

Table 1. Photophysical properties of Chemosensor **1**.

Chemosensor [1]	Em λ_{max} (nm)	Stoichiometry [2]	Φ [3]	K_d (μM)
MC(1)	605	*	*	*
MC(1)-Mg^{2+}	590	2:1 (0.33)	0.20	6.0
MC(1)-Ca^{2+}	605	2:1 (0.33)	0.06	18.7

[1] Measurements recorded at 25 °C in acetonitrile solvent, under ambient light conditions. [2] Stoichiometric ratio of chemosensor to metal ion determined from Job's plot (apex). [3] Relative fluorescence quantum yield determined in acetonitrile using Rhodamine B (Φ = 0.31) as a standard. * No data obtained.

The absorbance and fluorescence emission spectra for the fluorinated chemosensor **2** were similarly analysed. Fluorescence emission spectra gave two distinct emission maxima, which are attributable to the SP (~560 nm) and MC (~605 nm) isomers of chemosensor **2** [36] and suggest the

presence of both these species in solution (Figure S14), as per the earlier proton NMR spectrum. The chemosensor shows a similar fluorescence response in the presence of Mg^{2+} and Zn^{2+} with non-significant response for all other ions. In particular, a diminished fluorescence is observed in the presence of Ca^{2+} compared to chemosensor **1**. In all cases, while the presence of metal ions appears to affect the fluorescence intensity of chemosensor **2**, no shifts in the emission maxima are observed. Interestingly, chemosensor **2** exhibits no absorbance in the characteristic MC region and unlike chemosensor **1**, no absorbance was observed for the **2**-Cu^{2+} species (Figure S10). Job's plot analysis of chemosensor **2** suggests multiple potential binding stoichiometries may be present (Figure S15). Based on these results, subsequent optical fibre-based studies were only performed on chemosensor **1**. Finally, fluorescence emission spectra of the ester-protected precursors **3** and **4** revealed a loss of fluorescence intensity in the presence of all ions (see Figure S16), indicating that the free carboxylic acid (of **1** and **2**) is important for metal ion chelation, and hence chemosensor brightness and selectivity as per the earlier discussion and modelling results.

3.4. Photoswitching in an Optical Fibre

In the final part of the study, chemosensor **1** was combined with a microstructured optical fibre in order to demonstrate compatibility and as a first step in the development of a light-controlled, dip-sensor for Mg^{2+}. Photostability and photo-reversibility of analyte binding to **1** were defined on a silica-based, in-house fabricated suspended core optical fibre (SCF) [53,54], which allows rapid photoswitching using a laser. Interaction between the light and **1** in microstructured optical fibres is extended along the entire length of the fiber, while maintaining the integrity of the device. In SCFs, the glass core is suspended in air by thin struts, allowing a portion of the guided light to extend outside the fiber core into the surrounding holes which serve as low-volume sample chambers (see Figure 4A, schematic).

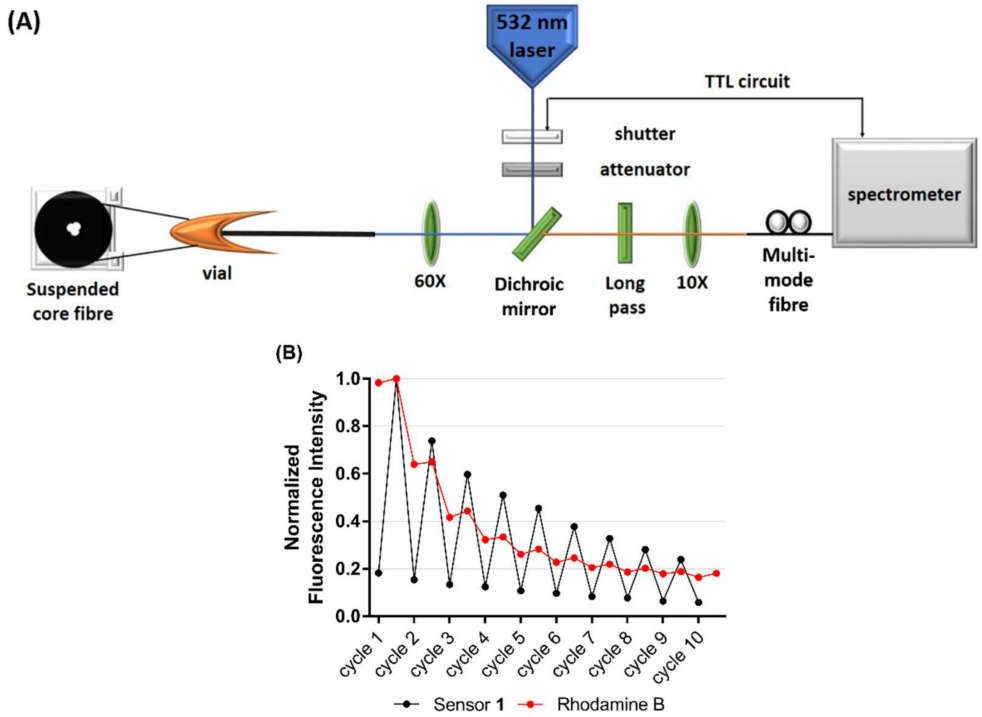

Figure 4. (**A**) Schematic of the optical setup used to measure fluorescence from a suspended core microstructured optical fibre (SCF). (**B**) Photostability of chemosensor **1** (500 μM) in the presence of Mg^{2+} (1 mM) (black), compared to the photostability of Rhodamine B (red) in an SCF. Excitation was at 532 nm, with 10 × 50 ms pulses at 1 mW power. Results are normalised to the highest fluorescence measurement, respectively.

Photoswitching between the weakly fluorescent SP isomer and the highly fluorescent MC(**1**)-Mg^{2+} complex was achieved by irradiation with UV ('on'-cycle, 365 nm lamp) and visible light ('off'-cycle, 532 nm green laser), respectively, within the SCF platform. A significant decrease in signal was observed in the first 4 experimental cycles, falling to 50% of the initial fluorescence, as seen in Figure 4B. This decrease is likely the result of the sensor switching back to the weakly-fluorescent SP isomer under the influence of the 532 nm laser light and/or light induced parasitic side reactions that led to the formation of non-switchable by-products, a process that is not completely understood and beyond the scope of this work [55]. In comparison, the fluorescence of Rhodamine B (a fluorophore capable of excitation under the same 532 nm laser but not photoswitchable) fell to 30% of the initial fluorescence by the same photoswitching cycle in a similar experiment. These results demonstrate that chemosensor **1** is capable of photoswitching over multiple cycles in the SCF platform, however future work is needed to optimise the laser power and intensity to reduce the initial photo-decolouration.

4. Conclusions

Here we present the rational design and photophysical characterisation of spiropyran-based chemosensors for Mg^{2+}, **1** and **2**. Fluorescence characterisation revealed that the C6'-nitro functionalised chemosensor **1** exhibits a 2-fold fluorescence enhancement factor for Mg^{2+} over Ca^{2+} ions, comparable to the commercially available mag-fura-2 [21]. Importantly, the dissociation constant (K_d) of **1**-Mg^{2+} was calculated to be 6.0 μM, with a 3-fold weaker affinity observed for **1**-Ca^{2+} (18.7 μM). As proposed by DFT modelling, stoichiometric studies support 2:1 chemosensor to metal ion binding of **1** with Mg^{2+}. Interestingly, structural and fluorescence characterisation of the C6'-fluorinated analogue **2** suggests the presence of both SP and MC species in solution, while stoichiometric studies indicate a complex metal binding relationship with Mg^{2+}. Subsequent studies were thus focused on **1**, which was combined with a suspended core optical fiber (SCF) as a first step towards the development of a light-controlled, reversible dip-sensor for Mg^{2+}. Fibre-based photoswitching experiments revealed reversible Mg^{2+} binding with improved photostability, as compared to the non-photoswitchable Rhodamine B fluorophore.

Supplementary Materials: The following are available online at http://www.mdpi.com/2227-9040/6/2/17/s1, Figures S1–S7: NMR spectra; Figure S8: HRMS spectra; Figure S9: DFT images of **2**; Figure S10: Absorbance spectra for **1** and **2**; Figure S11: Job's Plot of **1** with Ca^{2+}; Figure S12: Determination of K_d constants; Figure S13: Determination of Quantum Yield values; Figure S14: Fluorescence spectra of **2**; Figure S15: Job's Plot of **2** with Mg^{2+}; **Figure S16**: Selectivity profiles of **3** and **4**.

Acknowledgments: The authors (G.M.S., S.H., A.B., H.E.-H and A.D.A) acknowledge funding support from the Centre of Nanoscale BioPhotonics, through the Australian Research Council (ARC) CE140100 003. This work was performed in part at the OptoFab node of the Australian National Fabrication Facility utilising Commonwealth and South Australian State Government funding. The authors would like to acknowledge Yow Yu Ting and Nicole Tan Jia Ling for assistance with fluorescence characterisation. This work was supported with high-performance computing resources provided by the Phoenix HPC service at the University of Adelaide and the A*STAR Computational Resource Center (A*CRC).

Author Contributions: G.M.S., S.H. and A.D.A. conceived and designed the experiments; A.M.M. performed DFT calculations; G.M.S. synthesised and characterised all compounds; A.B. performed optical fibre experiments; G.M.S., S.H. and A.B. analysed data; H.E.-H. contributed analytical tools; G.M.S., S.H. and A.D.A. wrote the paper.

Conflicts of Interest: The authors declare no conflict of interest. The founding sponsors had no role in the design of the study; in the collection, analyses, or interpretation of data; in the writing of the manuscript, and in the decision to publish the results.

References

1. Glasdam, S.M.; Glasdam, S.; Peters, G.H. The importance of magnesium in the human body: A systematic literature review. *Adv. Clin. Chem.* **2016**, *73*, 169–193. [PubMed]
2. Wolf, F.I.; Trapani, V. Cell (patho)physiology of magnesium. *Clin. Sci.* **2008**, *114*, 27–35. [CrossRef] [PubMed]
3. Gunther, T. Concentration, compartmentation and metabolic function of intracellular free Mg^{2+}. *Magnes. Res.* **2006**, *19*, 225–236. [PubMed]

4. Romani, A.M. Cellular magnesium homeostasis. *Arch. Biochem. Biophys.* **2011**, *512*, 1–23. [CrossRef] [PubMed]
5. Ryan, M.F. The role of magnesium in clinical biochemistry: An overview. *Ann. Clin. Biochem.* **1991**, *28 Pt 1*, 19–26. [CrossRef] [PubMed]
6. Shi, J.; Krishnamoorthy, G.; Yang, Y.; Hu, L.; Chaturvedi, N.; Harilal, D.; Qin, J.; Cui, J. Mechanism of magnesium activation of calcium-activated potassium channels. *Nature* **2002**, *418*, 876–880. [CrossRef] [PubMed]
7. Mubagwa, K.; Gwanyanya, A.; Zakharov, S.; Macianskiene, R. Regulation of cation channels in cardiac and smooth muscle cells by intracellular magnesium. *Arch. Biochem. Biophys.* **2007**, *458*, 73–89. [CrossRef] [PubMed]
8. Nadler, M.J.; Hermosura, M.C.; Inabe, K.; Perraud, A.L.; Zhu, Q.; Stokes, A.J.; Kurosaki, T.; Kinet, J.P.; Penner, R.; Scharenberg, A.M.; et al. Ltrpc7 is a mg.Atp-regulated divalent cation channel required for cell viability. *Nature* **2001**, *411*, 590–595. [CrossRef] [PubMed]
9. Ko, Y.H.; Hong, S.; Pedersen, P.L. Chemical mechanism of atp synthase. Magnesium plays a pivotal role in formation of the transition state where atp is synthesized from adp and inorganic phosphate. *J. Biol. Chem.* **1999**, *274*, 28853–28856. [CrossRef] [PubMed]
10. Sarrafzadegan, N.; Khosravi-Boroujeni, H.; Lotfizadeh, M.; Pourmogaddas, A.; Salehi-Abargouei, A. Magnesium status and the metabolic syndrome: A systematic review and meta-analysis. *Nutrition* **2016**, *32*, 409–417. [CrossRef] [PubMed]
11. Mooren, F.C. Magnesium and disturbances in carbohydrate metabolism. *Diabetes Obes. Metab.* **2015**, *17*, 813–823. [CrossRef] [PubMed]
12. Volpe, S.L. Magnesium, the metabolic syndrome, insulin resistance, and type 2 diabetes mellitus. *Crit. Rev. Food Sci. Nutr.* **2008**, *48*, 293–300. [CrossRef] [PubMed]
13. Veronese, N.; Zurlo, A.; Solmi, M.; Luchini, C.; Trevisan, C.; Bano, G.; Manzato, E.; Sergi, G.; Rylander, R. Magnesium status in alzheimer's disease: A systematic review. *Am. J. Alzheimer's Dis. Other Dement.* **2016**, *31*, 208–213. [CrossRef] [PubMed]
14. Barbagallo, M.; Belvedere, M.; Di Bella, G.; Dominguez, L.J. Altered ionized magnesium levels in mild-to-moderate alzheimer's disease. *Magnes. Res.* **2011**, *24*, S115–S121. [PubMed]
15. Kolte, D.; Vijayaraghavan, K.; Khera, S.; Sica, D.A.; Frishman, W.H. Role of magnesium in cardiovascular diseases. *Cardiol. Rev.* **2014**, *22*, 182–192. [CrossRef] [PubMed]
16. Kupetsky-Rincon, E.A.; Uitto, J. Magnesium: Novel applications in cardiovascular disease–a review of the literature. *Ann. Nutr. Metab.* **2012**, *61*, 102–110. [CrossRef] [PubMed]
17. Geiger, H.; Wanner, C. Magnesium in disease. *Clin. Kidney J.* **2012**, *5*, i25–i38. [CrossRef] [PubMed]
18. Long, S.; Romani, A.M.P. Role of cellular magnesium in human diseases. *Austin J. Nutr. Food Sci.* **2014**, *2*, 1051. [PubMed]
19. Carter, K.P.; Young, A.M.; Palmer, A.E. Fluorescent sensors for measuring metal ions in living systems. *Chem. Rev.* **2014**, *114*, 4564–4601. [CrossRef] [PubMed]
20. Raju, B.; Murphy, E.; Levy, L.A.; Hall, R.D.; London, R.E. A fluorescent indicator for measuring cytosolic free magnesium. *Am. J. Physiol.-Cell Physiol.* **1989**, *256*, C540–C548. [CrossRef] [PubMed]
21. Fluorescent Mg2+ indicators. *The Molecular Probes Handbook—A Guide to Fluorescent Probes and Labeling Technologies*, 11st ed.; ThermoFisher Scientific: Waltham, MA, USA, 2010; pp. 862–864.
22. Levy, L.A.; Murphy, E.; Raju, B.; London, R.E. Measurement of cytosolic free magnesium ion concentration by fluorine-19 nmr. *Biochemistry* **1988**, *27*, 4041–4048. [CrossRef] [PubMed]
23. Schachter, M.; Gallagher, K.L.; Sever, P.S. Measurement of intracellular magnesium in a vascular smooth muscle cell line using a fluorescent probe. *Biochim. Biophys. Acta (BBA) Gen. Subj.* **1990**, *1035*, 378–380. [CrossRef]
24. Murphy, E.; Freudenrich, C.C.; Levy, L.A.; London, R.E.; Lieberman, M. Monitoring cytosolic free magnesium in cultured chicken heart cells by use of the fluorescent indicator furaptra. *Proc. Natl. Acad. Sci. USA* **1989**, *86*, 2981–2984. [CrossRef] [PubMed]
25. Grubbs, R.; Walter, A. Determination of cytosolic Mg^{2+} activity and buffering in BC3H-1 cells with MAG-fura-2. *Mol. Cell. Biochem* **1994**, *136*, 11–22. [CrossRef] [PubMed]
26. Martínez-Zaguilán, R.; Parnami, J.; Martinez, G.M. Mag-fura-2 (furaptra) exhibits both low (μm) and high (nm) affinity for Ca^{2+}. *Cell. Physiol. Biochem.* **1998**, *8*, 158–174. [CrossRef] [PubMed]

27. Hurley, T.W.; Ryan, M.P.; Brinck, R.W. Changes of cytosolic Ca^{2+} interfere with measurements of cytosolic Mg^{2+} using mag-fura-2. *Am. J. Physiol.-Cell Physiol.* **1992**, *263*, C300–C307. [CrossRef] [PubMed]
28. Shindo, Y.; Fujii, T.; Komatsu, H.; Citterio, D.; Hotta, K.; Suzuki, K.; Oka, K. Newly developed Mg^{2+}-selective fluorescent probe enables visualization of mg2+ dynamics in mitochondria. *PLoS ONE* **2011**, *6*, e23684. [CrossRef] [PubMed]
29. Komatsu, H.; Iwasawa, N.; Citterio, D.; Suzuki, Y.; Kubota, T.; Tokuno, K.; Kitamura, Y.; Oka, K.; Suzuki, K. Design and synthesis of highly sensitive and selective fluorescein-derived magnesium fluorescent probes and application to intracellular 3d Mg^{2+} imaging. *J. Am. Chem. Soc.* **2004**, *126*, 16353–16360. [CrossRef] [PubMed]
30. Matsui, Y.; Sadhu, K.K.; Mizukami, S.; Kikuchi, K. Highly selective tridentate fluorescent probes for visualizing intracellular Mg^{2+} dynamics without interference from Ca^{2+} fluctuation. *Chem. Commun.* **2017**, *53*, 10644–10647. [CrossRef] [PubMed]
31. Trapani, V.; Farruggia, G.; Marraccini, C.; Iotti, S.; Cittadini, A.; Wolf, F.I. Intracellular magnesium detection: Imaging a brighter future. *Analyst* **2010**, *135*, 1855–1866. [CrossRef] [PubMed]
32. Trapani, V.; Schweigel-Rontgen, M.; Cittadini, A.; Wolf, F.I. Intracellular magnesium detection by fluorescent indicators. *Methods Enzymol.* **2012**, *505*, 421–444. [PubMed]
33. Natali, M.; Giordani, S. Interaction studies between photochromic spiropyrans and transition metal cations: The curious case of copper. *Org. Biomol. Chem.* **2012**, *10*, 1162–1171. [CrossRef] [PubMed]
34. Natali, M.; Giordani, S. Molecular switches as photocontrollable "smart" receptors. *Chem. Soc. Rev.* **2012**, *41*, 4010–4029. [CrossRef] [PubMed]
35. Lukyanov, B.S.; Lukyanova, M.B. Spiropyrans: Synthesis, properties, and application. *Chem. Heterocycl. Compd.* **2005**, *41*, 281–311. [CrossRef]
36. Klajn, R. Spiropyran-based dynamic materials. *Chem. Soc. Rev.* **2014**, *43*, 148–184. [CrossRef] [PubMed]
37. Zakharova, M.I.; Pimienta, V.; Metelitsa, A.V.; Minkin, V.I.; Micheaua, J.C. Thermodynamic and kinetic analysis of metal ion complexation by photochromic spiropyrans. *Russ. Chem. Bull.* **2009**, *58*, 1329–1337. [CrossRef]
38. Heng, S.; Mak, A.M.; Kostecki, R.; Zhang, X.Z.; Pei, J.X.; Stubing, D.B.; Ebendorff-Heidepriem, H.; Abell, A.D. Photoswitchable calcium sensor: 'On'-'off' sensing in cells or with microstructured optical fibers. *Sens. Actuators B Chem.* **2017**, *252*, 965–972. [CrossRef]
39. Heng, S.; McDevitt, C.A.; Kostecki, R.; Morey, J.R.; Eijkelkamp, B.A.; Ebendorff-Heidepriem, H.; Monro, T.M.; Abell, A.D. Microstructured optical fiber-based biosensors: Reversible and nanoliter-scale measurement of zinc ions. *ACS Appl. Mater. Interfaces* **2016**, *8*, 12727–12732. [CrossRef] [PubMed]
40. Heng, S.; Nguyen, M.-C.; Kostecki, R.; Monro, T.M.; Abell, A.D. Nanoliter-scale, regenerable ion sensor: Sensing with a surface functionalized microstructured optical fibre. *RSC Adv.* **2013**, *3*, 8308–8317. [CrossRef]
41. Stubing, D.B.; Heng, S.; Monro, T.M.; Abell, A.D. A comparative study of the fluorescence and photostability of common photoswitches in microstructured optical fibre. *Sens. Actuators B Chem.* **2017**, *239*, 474–480. [CrossRef]
42. Monro, T.M.; Warren-Smith, S.; Schartner, E.P.; François, A.; Heng, S.; Ebendorff-Heidepriem, H.; Afshar, S. Sensing with suspended-core optical fibers. *Opt. Fiber Technol.* **2010**, *16*, 343–356. [CrossRef]
43. Schartner, E.P.; Henderson, M.R.; Purdey, M.; Dhatrak, D.; Monro, T.M.; Gill, P.G.; Callen, D.F. Cancer detection in human tissue samples using a fiber-tip pH probe. *Cancer Res.* **2016**, *76*, 6795–6801. [CrossRef] [PubMed]
44. Purdey, M.S.; Schartner, E.P.; Sutton-McDowall, M.L.; Ritter, L.J.; Thompson, J.; Monro, T.M.; Abell, A.D. Localised hydrogen peroxide sensing for reproductive health. In Proceedings of the SPIE Optics + Optoelectronics, Prague, Czech Republic, 13–16 April 2015.
45. Collins, G.E.; Choi, L.-S.; Ewing, K.J.; Michelet, V.; Bowen, C.M.; Winkler, J.D. Photoinduced switching of metal complexation by quinolinospiropyranindolines in polar solvents. *Chem. Commun.* **1999**, 321–322. [CrossRef]
46. Garcia, A.A.; Cherian, S.; Park, J.; Gust, D.; Jahnke, F.; Rosario, R. Photon-controlled phase partitioning of spiropyrans. *J. Phys. Chem. A* **2000**, *104*, 6103–6107. [CrossRef]
47. Baldrighi, M.; Locatelli, G.; Desper, J.; Aakeroy, C.B.; Giordani, S. Probing metal ion complexation of ligands with multiple metal binding sites: The case of spiropyrans. *Chem.-Eur. J.* **2016**, *22*, 13976–13984. [CrossRef] [PubMed]

48. Heng, S.; Mak, A.M.; Stubing, D.B.; Monro, T.M.; Abell, A.D. Dual sensor for cd(ii) and ca(ii): Selective nanoliter-scale sensing of metal ions. *Anal. Chem.* **2014**, *86*, 3268–3272. [CrossRef] [PubMed]
49. Filley, J.; Ibrahim, M.A.; Nimlos, M.R.; Watt, A.S.; Blake, D.M. Magnesium and calcium chelation by a bis-spiropyran. *J. Photochem. Photobiol. A Chem.* **1998**, *117*, 193–198. [CrossRef]
50. Becke, A.D. Density-functional thermochemistry. III. The role of exact exchange. *J. Chem. Phys.* **1993**, *98*, 5648–5652. [CrossRef]
51. Frisch, M.J.E.A. *Gaussian 09*; Gaussian, Inc.: Wallingford, CT, USA, 2009.
52. Magde, D.; Rojas, G.E.; Seybold, P.G. Solvent dependence of the fluorescence lifetimes of xanthene dyes. *Photochem. Photobiol.* **1999**, *70*, 737–744. [CrossRef]
53. Zhao, J.B.; Jin, D.Y.; Schartner, E.P.; Lu, Y.Q.; Liu, Y.J.; Zvyagin, A.V.; Zhang, L.X.; Dawes, J.M.; Xi, P.; Piper, J.A.; et al. Single-nanocrystal sensitivity achieved by enhanced upconversion luminescence. *Nat. Nanotechnol.* **2013**, *8*, 729–734. [CrossRef] [PubMed]
54. Schartner, E.P.; Tsiminis, G.; Francois, A.; Kostecki, R.; Warren-Smith, S.C.; Nguyen, L.V.; Heng, S.; Reynolds, T.; Klantsataya, E.; Rowland, K.J.; et al. Taming the light in microstructured optical fibers for sensing. *Int. J. Appl. Glass Sci.* **2015**, *6*, 229–239. [CrossRef]
55. Wiedemann, U.; Alt, W.; Meschede, D. Switching photochromic molecules adsorbed on optical microfibres. *Opt. Express* **2012**, *20*, 12710–12720. [CrossRef] [PubMed]